

# Tremella derived ultrahigh specific surface area activated carbon for high performance supercapacitor



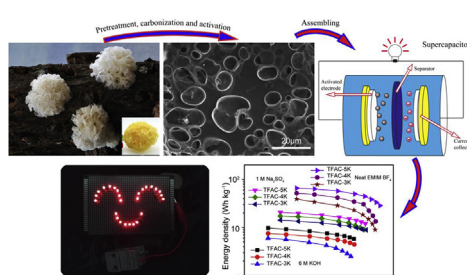
Nannan Guo, Min Li, Xingkai Sun, Feng Wang\*, Ru Yang\*\*

State Key Laboratory of Chemical Resource Engineering, Beijing Key Laboratory of Electrochemical Process and Technology for Materials, Beijing University of Chemical Technology, Beijing 100029, PR China

## HIGHLIGHTS

- Activated carbons are prepared by carbonization and KOH-activation of available biomass tremella.
- The activated carbons possess ultrahigh specific surface area ( $3760 \text{ m}^2 \text{ g}^{-1}$ ).
- High specific capacitance ( $71 \text{ F g}^{-1}$ ) detected in two-electrode systems.
- High energy density:  $65.6 \text{ W h kg}^{-1}$  at the power density of  $743 \text{ W kg}^{-1}$ .

## GRAPHICAL ABSTRACT



## ARTICLE INFO

### Article history:

Received 15 May 2017

Received in revised form

13 July 2017

Accepted 20 August 2017

Available online 23 August 2017

### Keywords:

Tremella

Ultrahigh specific surface area

Activated carbon

Supercapacitor

## ABSTRACT

Activated carbons derived from sustainable biomass have attracted widespread attention as electrode materials for supercapacitors due to their economic value, tunable physical/chemical properties and environmental concern. Tremella, renewable and abundant biomass, has been explored as precursor to prepare hierarchical activated carbons by means of carbonization and KOH activation. The obtained sample possesses an ultrahigh BET specific surface area of  $3760 \text{ m}^2 \text{ g}^{-1}$  and very high mesopore volume ratio of 72%. So, the sample shows a superior specific capacitance  $71 \text{ F g}^{-1}$  at  $1 \text{ A g}^{-1}$ ; extraordinary rate performance with a capacitance of  $53.5 \text{ F g}^{-1}$  at  $30 \text{ A g}^{-1}$ ; outstanding cycle stability with 99% capacitance retention after 10,000 galvanostatic charge-discharge cycles at  $5 \text{ A g}^{-1}$  in a symmetric two-electrode supercapacitor with 6 M KOH solution as electrolyte. The assembled supercapacitor shows a superior energy density of  $65.6 \text{ W h kg}^{-1}$  in ionic liquid electrolyte system and  $28 \text{ W h kg}^{-1}$  is still maintained even at an ultrahigh power density  $19,700 \text{ W kg}^{-1}$ .

© 2017 Elsevier B.V. All rights reserved.

## 1. Introduction

Considering the challenges of excessive depletion of fossil fuels, the global warming and growing population, green and sustainable energy technologies have attracted more and more attentions for

future energy storage, conversion and usage [1–7]. Among various energy storage systems, supercapacitors (SCs) possess larger energy density than traditional capacitors and can deliver a much higher power density compared with conventional batteries [8]. According to the different energy storage mechanism, SCs can be classified into electric pseudo-capacitors transporting electrolyte ions by reversible faradaic reactions and double-layer capacitors (EDLCs) accumulating charged ions in the electrical double layer [8–12]. Pseudo-capacitors can deliver much higher capacitance

\* Corresponding author.

\*\* Corresponding author.

E-mail addresses: [wangf@mail.buct.edu.cn](mailto:wangf@mail.buct.edu.cn) (F. Wang), [ruyang@mail.buct.edu.cn](mailto:ruyang@mail.buct.edu.cn) (R. Yang).

than EDLCs. However, EDLCs is the majority of currently available commercial SCs, mainly attributed to their long cycle-life, high power density and technical maturity [3].

The energy density of EDLCs is proportional to the square of voltage window and the capacitance according to the equation  $E = CV^2/2$  [9]. Therefore, exploiting high performance electrode materials to improve the capacitance and electrolytes to enhance the operating voltage are of particular significance. Ionic liquids have been regarded as a promising electrolytes of EDLCs due to their higher operating voltage ( $>3$  V), nonflammability, negligible volatility and excellent electrochemical/thermal stability [13–17]. Tian et al. found that the operating voltage in EMIM TFSI electrolyte can reach to 3.5 V [18]. Wang et al. reported that the operating voltage in EMIM  $BF_4$  can even reach to 4 V [19].

Among the various electrode materials being considered for EDLCs, carbon materials including activated carbons (AC) [20–23], carbon nanotubes [24,25], templated carbons [26,27], carbon aerogels [28,29] and graphene [30–32] are commonly studied owing to their high specific surface area (SSA), tunable porosity, good stability, favorable electrical conductivity and environmental comparability [3]. However, carbon nanotubes, graphene and carbon aerogels suffer from high cost and harsh preparation conditions for scalable production [33]. So, AC is greatly used to assemble commercial SCs owing to its relatively low cost, sustainable precursors, well-developed manufacturing technologies and easy production in large quantities [1].

To achieve high SCs performance, the AC should have high SSA accumulating more electrolyte ions at interface of electrode/electrolyte and well-distributed hierarchical pores structure enhancing the ionic transport in electrode materials to promote the specific capacitance [34–36]. Recently, abundant and renewable biomass wastes have attracted much attention due to the excessive consumption of fossil fuels and environmental concern [1,37]. To date, various biomass-derived ACs have been prepared for high performance EDLCs electrodes [38–45]. For example, Guo et al. prepared 3D hierarchical porous carbon by facile carbonization and KOH activation of soybeans roots [38]. The as-prepared material possessing large specific surface area ( $2143\text{ m}^2\text{ g}^{-1}$ ) and good electrical conductivity shows high capacitance ( $69\text{ F g}^{-1}$  at  $0.5\text{ A g}^{-1}$ ), superior cycle durability (98% capacitance retention after 10,000 cycles), and good rate performance in symmetric two-electrode SC in 6 M KOH. Tan et al. reported the preparation of AC materials from two the seeds of platanus and willow. The symmetric device of these two samples with 6 M KOH electrolyte display high capacitance of 71.6 and  $66.9\text{ F g}^{-1}$  at  $0.25\text{ A g}^{-1}$ , and 97.03% and 91.12% capacity retention after 10,000 cycles, respectively [40].

Tremella, also known as white fungus, is one of the most common fungi and abundant in nature, its appearance similar to black fungus with only color difference [46]. The chemical composition of tremella mainly contains heteropolysaccharide, butcher wall polysaccharide and exo-poly saccharides [47]. In this work, ACs was obtained by carbonization and KOH-activation of available biomass tremella fuciformis. Influences of KOH/C ratio on the surface chemistry and pore structure are systematically studied. The as-prepared sample possesses ultrahigh BET SSA of  $3760\text{ m}^2\text{ g}^{-1}$  and high content of surface oxygen. So, the sample shows very high specific capacitance, superior cycle stability and good rate performance in a symmetric two-electrode EDLC in 6 M KOH (1 V), 1 M  $Na_2SO_4$  (1.6 V) and neat EMIM  $BF_4$  (3 V).

## 2. Experimental

### 2.1. Preparation of tremella based ultrahigh SSA activated carbon

Tremella was purchased from the supermarket in Beijing. Firstly,

the tremella was washed by ultrapure water and dried at  $80^\circ\text{C}$ . The clean tremella was heated in a tube furnace at  $400^\circ\text{C}$  (heating rate,  $5^\circ\text{C min}^{-1}$ ) for 2 h under high purity nitrogen atmosphere. The obtained char was denoted as TF-400. The TF-400 and KOH were mixed at different KOH/C ratio (3, 4 and 5) in agate mortar, then the mixture was activated at  $800^\circ\text{C}$  for 3 h under nitrogen flow in a tube furnace. The obtained black powder was washed by HCl solution (5 wt%) and subsequently washed by ultrapure water. Finally, the as-prepared sample was dried in an oven at  $80^\circ\text{C}$  for 12 h. These tremella-derived ACs were named as TFAC-nK, where n indicates the different KOH/C ratio.

### 2.2. Characterization

The surface morphology of the as-prepared ACs was characterized with scanning electron microscope (SEM, Hitachi S-4800). The degree of graphitization was measured by Raman spectroscopy (Renishaw, InViaReflex). The bulk elementary composition of TFAC was characterized by an Elementar vario EL CUBE (Elemental Analyse system GmbH). The surface atomic content was measured by X-ray photoelectron spectra (XPS, Thermo ESCALAB250). Electrical conductivity of the samples was measured by four-probed method at a pressure of 10 MPa on a Hall effect measurement system (RH2030, PhysTech). Surface area and porosity was characterized by Nitrogen adsorption-desorption analyzer (Micromeritics, ASAP2020).

### 2.3. Electrochemical characterization

The working electrode was prepared by the TFAC, polytetrafluoroethylene (PTFE) and acetylene black at a mass ratio of 8:1:1 in absolute ethyl alcohol. Then the mixture was stirred 12 h and pressed onto nickel foam. The mass of the TFAC loading on the working electrode was approximately  $3\text{ mg cm}^{-2}$ . Two dried working electrodes were constructed in a 2032 stainless steel coin cell by using a nonwoven polypropylene mat (MPF 30AC) as the membrane in 6 M KOH (1 V), 1 M  $Na_2SO_4$  (1.6 V) and neat EMIM  $BF_4$  (3 V) as the electrolyte. Galvanostatic charge-discharge (GCD), electrochemical impedance spectroscopy (EIS) and cyclic voltammetry (CV) curves were obtained by electrochemical work station (CHI 760E, China). In this work, the specific capacitances (C) of the TFAC based two-electrode SCs were calculated based on equation (1) [3]:

$$C = I\Delta t/2m\Delta V \quad (1)$$

Where  $I$  represents the discharge current,  $\Delta t$  refer to the discharge time,  $m$  is the mass of TFAC loaded on a single working electrode and  $\Delta V$  is the operating voltage except the ohmic drop. Energy and power density of the TFAC based two-electrode cells were calculated using equations (2) and (3) [3]:

$$E = CV^2/2 \times 3.6 \quad (2)$$

$$P = E/3600\Delta t \quad (3)$$

## 3. Results and discussion

Due to its fast growth rate and scalable preparation as seen in Fig. 1a, tremella is a promising precursor for ACs [46]. The typical SEM images of TF-400 and TFAC-5K are presented in Fig. 1. A lot of complete or incomplete hole expose on the surface and inner of TF-400 in Fig. 1b, the hole may provide effective places for the

activating reaction during the activation process [38]. The surface becomes rough and the “valley” structure was generated after KOH etching, seen in Fig. 1c, d, e and f. The irregular and rough surface stature of carbon materials suggesting that KOH activation is conducive to the formation of porous texture. In addition, some volatile substances of the raw material decompose in pyrolysis process. The escape of gas can also effectively modify the surface morphology [48].

ACs with a large SSA and optimized pores structure are in great demand for the electrodes of EDLCs [49]. Fig. 2a exhibits the nitrogen adsorption-desorption isotherms of TF-400 and TFAC. TF-400 exhibits a very low quantity adsorbed, indicating an imporous characteristic. These isotherms with evident plateaus of TFAC belong to type I in the IUPAC classification [50]. The quantity absorbed ability is evidently developed and the knee of isotherm gradually becomes broad with the increasing KOH/C weight ratio from 3 to 5, indicating the increase of SSA and the wide of the pore size due to the activation of KOH [41]. In addition, broad and hysteresis loops at  $0.4 < P/P_0 < 0.8$  of TFAC-5K can be clearly observed, which clearly suggests wide pore size distributions because micropores are widened at higher KOH/C weight ratio [50]. Fig. 2b exhibits the corresponding pore size distributions of TF-400 and TFAC. TFAC-5K shows a broad pore size ranging from 0.5 nm to 6 nm and high ratio of mesopore volume. The volume of micropores (especially the pores less than 1 nm) decreases, while the volume of mesopores increases since the enhanced KOH activation can create and enlarge pores [38]. The structure parameters of TF-400 and TFAC are shown in Table 1. TF-400 shows undeveloped pore structure with a very low BET SSA ( $36.8 \text{ m}^2 \text{ g}^{-1}$ ) and pore volume ( $0.04 \text{ cm}^3 \text{ g}^{-1}$ ). However, BET SSA of TFAC dramatically increase from  $2220 \text{ m}^2 \text{ g}^{-1}$  to  $3760 \text{ m}^2 \text{ g}^{-1}$  and total pore volumes increase from  $0.98$  to  $2.15 \text{ cm}^3 \text{ g}^{-1}$  when the KOH/C ratio rises from 3 to 5. The mesopore volume ratio of TFAC-5K is 72%, which is much higher than that of TFAC-4K (39%) and TFAC-3K (14%). At low KOH/C ratio ( $<4$ ), the total pore volume increases mainly attributed to the generation of micropores, while the mesopore volume is a modest rise. Further increasing the ratio leads to a decrease of micropore volume and drastic rise of mesopore volume, indicating that high KOH/C ratio could result in the collapse of micropores and formation of small mesopores [38]. Thus, TFAC-5K, possessing the highest SSA and largest mesopore volume, is expected to display excellent EDLC performance as electrode material.

Although developed porous structure can provide favorable

diffusion channels and high SSA for electrolyte ions, it always leads to low graphitization degree and poor electrical conductivity, which is unfavorable for the transfer of electrons [9]. To identify the graphitic property of the TF-400 and TFAC, Raman spectra was characterized and exhibited in Fig. 2c. According to the spectra, two obvious broad bands locate at  $\sim 1351$  and  $\sim 1590 \text{ cm}^{-1}$ , representing the D band (disordered carbon) and the G band (graphitic), respectively. The intensity ratio of these peaks ( $I_D/I_G$ ) relies on the degree of graphitization. The lower the degree of graphitization, the higher is the ratio. TF-400 shows a low  $I_D/I_G$  (0.79) due to the undeveloped porous structure. All the  $I_D/I_G$  ratios of TFAC are nearly to 1, which suggests the amorphous carbon in the as-prepared TFAC. The  $I_D/I_G$  values are 0.89, 0.92, and 0.95 for TFAC-3K, TFAC-4K and TFAC-5K, suggesting a trade-off relationship between the pore structure and graphitization degree. So, the conductivity of TFAC-5K is  $1.23 \text{ S cm}^{-1}$ , which is lower than that of TFAC-3K ( $2.71 \text{ S cm}^{-1}$ ) and TFAC-4K ( $1.71 \text{ S cm}^{-1}$ ).

Elemental analysis was measured to investigate bulk composition of the raw tremella, TF-400 and TFAC. As seen in Table S1, the raw tremella contains 0.5 wt% sulfur, 0.6 wt% nitrogen, 8.0 wt% hydrogen, 45.7 wt% oxygen and 44.2 wt% carbon. After carbonization and KOH activation, the carbon content continuously increases to 93.8 wt% and the oxygen content drop to 4.1 wt%. Moreover, the small amount of nitrogen and sulfur in the carbon skeleton can modify the conduction band and improve the conductivity of TFAC, seen in Table S1 [51,52]. Surface atomic composition was further measured by XPS measurements. The surface atomic composition of TF-400 shows same trend to the bulk composition (Fig. 2d and Table S1). However, the surface oxygen content TFAC shows a reverse trend to the bulk content. The surface oxygen increased from 7.2 to 13.2 at.% with KOH/C ratio increase from 3 to 5. This may be attributed to high KOH/C enables more surface carbon atoms to be activated, which can capture more oxygen to form activated functionalities [53]. As seen in Fig. 2e, f and Fig. S1, the C1s spectrum exhibit four individual peaks at approximately 288.3, 286.2, 285.2 and  $284.7 \text{ eV}$  representing C=O, C-O,  $\text{sp}^3\text{-C}$  and  $\text{sp}^2\text{-C}$ , respectively [44]. The oxygen can be classified into three peaks at  $532.4 \text{ eV}$  (keto oxygen or quinone group, O-I),  $533.2 \text{ eV}$  (esters or phenolic group, O-II) and  $535.5 \text{ eV}$  (carboxylic group or water, O-III), respectively [41]. The species of O-I are considered to give rise to pseudo-capacitance effects [54,55]. Moreover, the surface oxygen groups can boost the wettability of AC materials [54,55].

Considering the high BET SSA, large mesopores ratio and

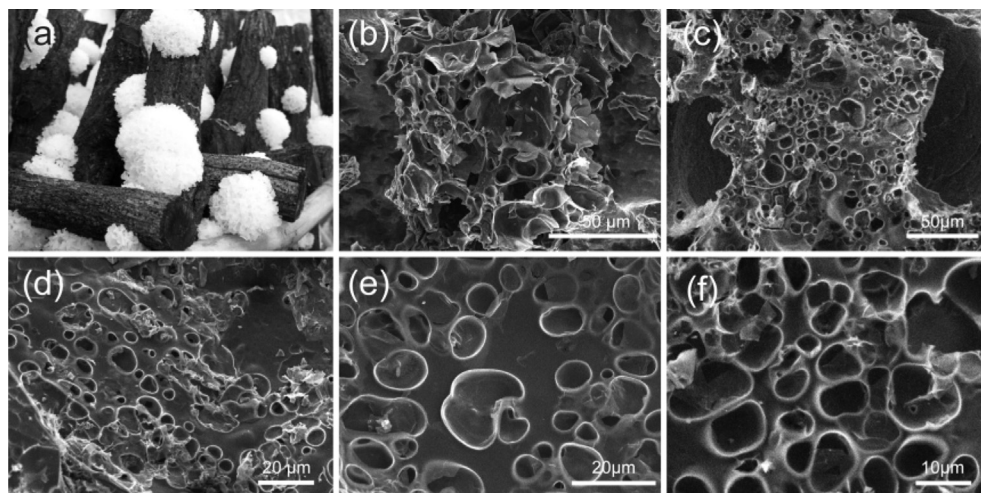
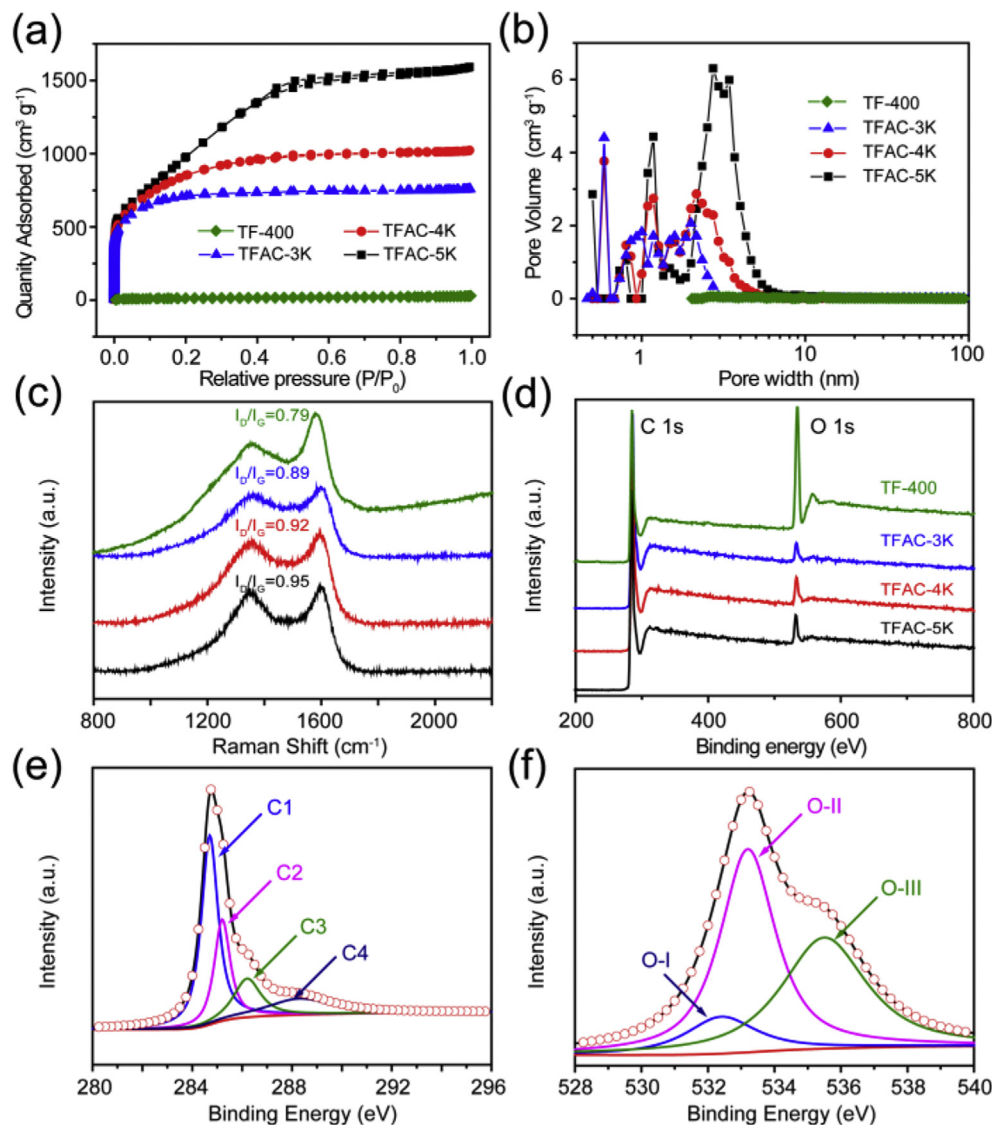


Fig. 1. (a) Digital photograph of the scalable preparation of tremella; (b) SEM images of TF-400; and (c, d, e, f) SEM images of TFAC-5K.



**Fig. 2.** (a) Nitrogen adsorption-desorption isotherms; (b) different pore size distribution of the TF-400 and TFAC; (c) Raman spectra; (d) XPS spectra of and TF-400 and TFAC; (e) C 1s spectra and (f) O1s of TFAC-5K.

**Table 1**

Textual Parameters and conductivity of the TF-400 and TFAC.

Samples	<sup>a</sup> $S_{BET}$ (m <sup>2</sup> /g)	<sup>b</sup> $S_t$ (m <sup>2</sup> /g)	<sup>c</sup> $S_{micro}$ (m <sup>2</sup> /g)	<sup>d</sup> $S_{meso}$ (m <sup>2</sup> /g)	<sup>e</sup> $V_t$ (cm <sup>3</sup> /g)	<sup>f</sup> $V_{micro}$ (cm <sup>3</sup> /g)	<sup>g</sup> $V_{meso}$ (cm <sup>3</sup> /g)	Conductivity (S/cm)
TF-400	36.8	11.6	0.3	8.4	0.04	0.01	0.03	—
TFAC-3K	2220	1822	1711	110	0.98	0.84	0.14	2.71
TFAC-4K	2840	1965	1576	389	1.34	0.82	0.52	1.71
TFAC-5K	3760	2216	1212	1004	2.15	0.60	1.55	1.23

<sup>a</sup> BET surface area.

<sup>b</sup> Total specific surface area obtained by DFT.

<sup>c</sup> Micropore (micro < 2 nm) surface area calculated by DFT.

<sup>d</sup> Mesopore (2 nm < meso < 50 nm) surface area calculated by DFT.

<sup>e</sup> Total pore volume obtained by DFT.

<sup>f</sup> Micropore volume calculated by DFT.

<sup>g</sup> Mesopore volume calculated by DFT.

abundant surface oxygen content, the electrochemical property of TFAC as SC electrodes are expectable. To evaluate the potential of the TFAC, their performance as SC electrodes was first measured in 6 M KOH. Fig. 3a exhibits the CV curves of TFAC-based SCs at

50 mV s<sup>-1</sup>. The quasi-rectangular CV curves of all samples indicate ideal EDLC nature of the charge and discharge process. These CV curves also exhibit a part deviation from the rectangular shape, implying the pseudo-capacitance induced by the surface



heteroatom functional groups [38]. Moreover, TFAC-5K exhibits the largest shape, indicating the highest specific capacitance. The excellent capacitive behavior of TFAC-5K based SC is also reflected in their symmetrical isosceles triangle-like charge-discharge profiles (Fig. 3b). TFAC-5K shows the longest discharge time, which is accordance with the result of CVs. This is also confirmed by Fig. 3c, which exhibits the impact of the discharge current on the specific capacitance. TFAC-5K based SC displays the largest specific capacitance of  $71 \text{ F g}^{-1}$  at  $1 \text{ A g}^{-1}$ , much higher than TFAC-4K ( $54.5 \text{ F g}^{-1}$ ), TFAC-3K ( $43.8 \text{ F g}^{-1}$ ) and most previously reported ACs in  $6 \text{ M KOH}$  (Table S2). Compared with these ACs, the high performance of TFAC-5K is attributed to the ultrahigh SSA, large mesopores volume ratio and abundant surface oxygen group. TFAC-5K also exhibits the highest capacitance retention (75.4%) at  $30 \text{ A g}^{-1}$ , suggesting excellent rate performance. Moreover, the capacitance still maintain at  $53.5 \text{ F g}^{-1}$ , which is much higher than TFAC-4K and TFAC-3K. The ideal capacitive behaviors of TFAC-5K based SC is also reflected in their quasi-rectangular CV curves and triangular GCD profiles (Fig. 3 and Fig. S2). The CV curve (Fig. 3d) retains almost rectangular even at  $500 \text{ mV s}^{-1}$ . The GCD curve also keeps triangle-like shape even at  $30 \text{ A g}^{-1}$ , which further demonstrate the good rate electrochemical performance of the TFAC-5K based electrode. Furthermore, long cycling performance of TFAC-5K based cell was also measured using the GCD at  $5 \text{ A g}^{-1}$ . The specific capacitance retention is 99% after 10,000 cycles in Fig. 3f, suggesting outstanding electrochemical stability and highly reversible ability during the charge and discharge process. The almost similar curve of the 1st cycles and the 10000th cycles also displays excellent stable cyclic ability (inset in Fig. 3f).

Further electrochemical characterization of TFAC based two-electrode cell system was tested in  $1 \text{ M Na}_2\text{SO}_4$ . As seen in Fig. S3a and b, such SC can reversibly cycle in a high voltage window of  $1.6 \text{ V}$ . This widening of the voltage window in  $1 \text{ M Na}_2\text{SO}_4$  is critical to achieve significant enhancement of the energy density based on the equation  $E = CV^2/2$ . Similarly, the largest CV curve

(Fig. 4a and Fig. S4) at different scan rates and longest discharge time (Fig. 4b and Fig. S4) at different current densities also confirm the best electrochemical performance of TFAC-5K based symmetric SC in  $1 \text{ M Na}_2\text{SO}_4$ . The specific capacitance of TFAC-5K is  $60 \text{ F g}^{-1}$  at  $0.5 \text{ A g}^{-1}$ , as seen in Fig. 4c. Up to  $30 \text{ A g}^{-1}$ , this result still maintain at 77.5% ( $46.5 \text{ F g}^{-1}$ ). CV and GCD curves further suggest the superior rate performance of the TFAC-5K based SCs in  $1 \text{ M Na}_2\text{SO}_4$  seen in Fig. 4d and e. The capacitance of TFAC-5K also possess 94% capacitance retention even suffered from 10,000 cycles at  $5 \text{ A g}^{-1}$ , indicating their excellent electrochemical durability (Fig. 4f).

Although the operating voltage can reach to  $1.6 \text{ V}$  in  $1 \text{ M Na}_2\text{SO}_4$ , it cannot fully meet the growing need of the high energy density. To widen the operating voltage, we also assembled TFAC based two-electrode SCs in neat EMIM  $\text{BF}_4$ . As seen in Fig. S3c and d, such SCs can reversibly operate at a much higher voltage window of  $3 \text{ V}$ . As seen in Fig. 5a and b and Fig. S5, all GCD and CV curves exhibit isosceles triangle and rectangular shapes, suggesting outstanding reversibility and ideal EDLC behavior. In addition, TFAC-5K also exhibits the largest current response and CV curves shapes. So, TFAC-5K displays the highest specific capacitance ( $53.3 \text{ F g}^{-1}$ ) at  $1 \text{ A g}^{-1}$ , while this result keeps 66.7% retention at  $30 \text{ A g}^{-1}$ , which is better than those of TFAC-3K, TFAC-4K and previously reported ACs in ionic liquids (Table S3). GCD profiles of TFAC-5K exhibit isosceles triangle shape even at  $50 \text{ A g}^{-1}$ , and CV curves also display quasi-rectangle shape even at  $400 \text{ mV s}^{-1}$ , further proving the superior electrochemical reversibility in neat EMIM  $\text{BF}_4$  (Fig. 5d and e). After 2500 cycles at  $5 \text{ A g}^{-1}$ , this SC shows 90% capacitance retention compared with the initial value (Fig. 5f). Compare with the device in aqueous system, the inferior rate and cycle performance is mainly attributed to the low ionic diffusivity and conductivity of ionic liquids [56]. Fig. 5f shows red LEDs ( $3 \text{ V}$ ) lit by symmetric TFAC-5K based SC in EMIM  $\text{BF}_4$ . This experiment further demonstrates the great potential of TFAC-5K for high performance SCs. The excellent electrochemical property of TFAC-5K can be attributed to two reasons: (1) high SSA can provide rich sites for charge

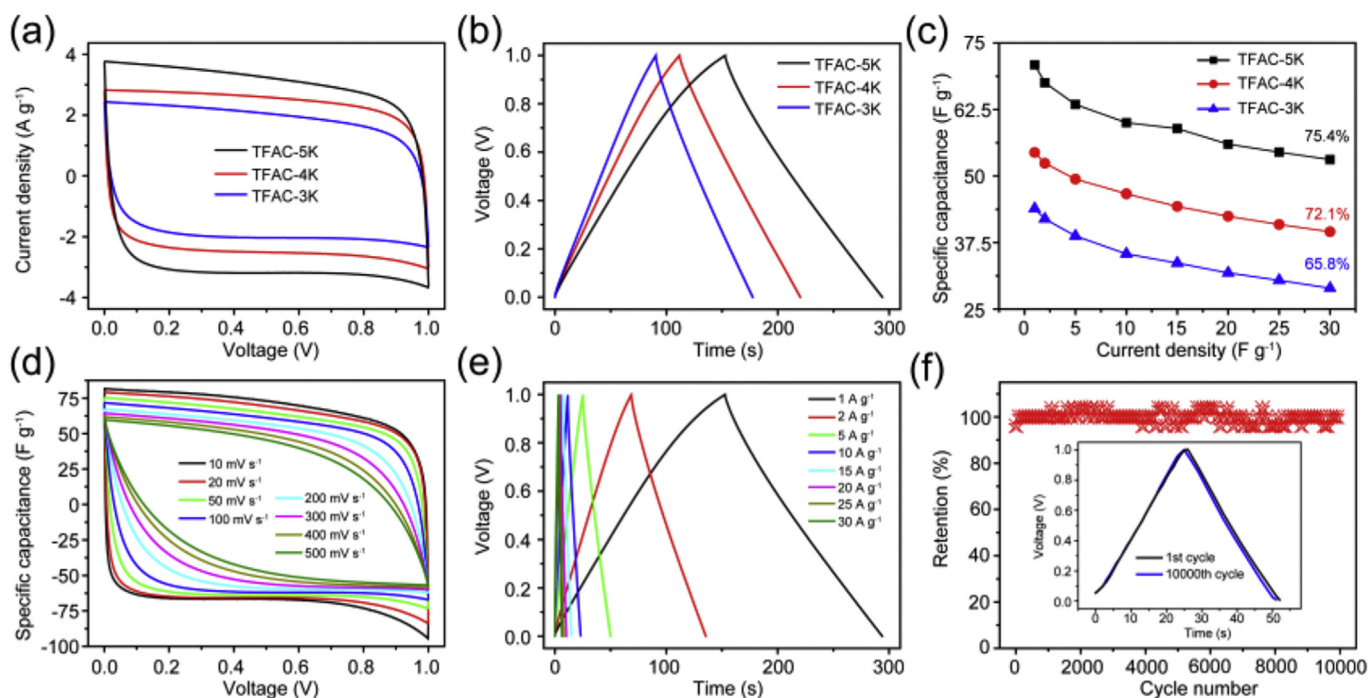


**Fig. 3.** (a) CV curves at  $50 \text{ mV s}^{-1}$ ; (b) GCD curves at  $2 \text{ A g}^{-1}$ ; (c) GCD rate performance of TFAC-3K, TFAC-4K and TFAC-5K in a symmetric two-electrode supercapacitor in  $6 \text{ M KOH}$  aqueous solution; (d) CV curves at different sweep rates; (e) GCD curves at different current densities; (f) cyclic durability at  $5 \text{ A g}^{-1}$  for 10,000 cycles of TFAC-5K (inset: GCD curves of the 1st and 10,000th cycles).

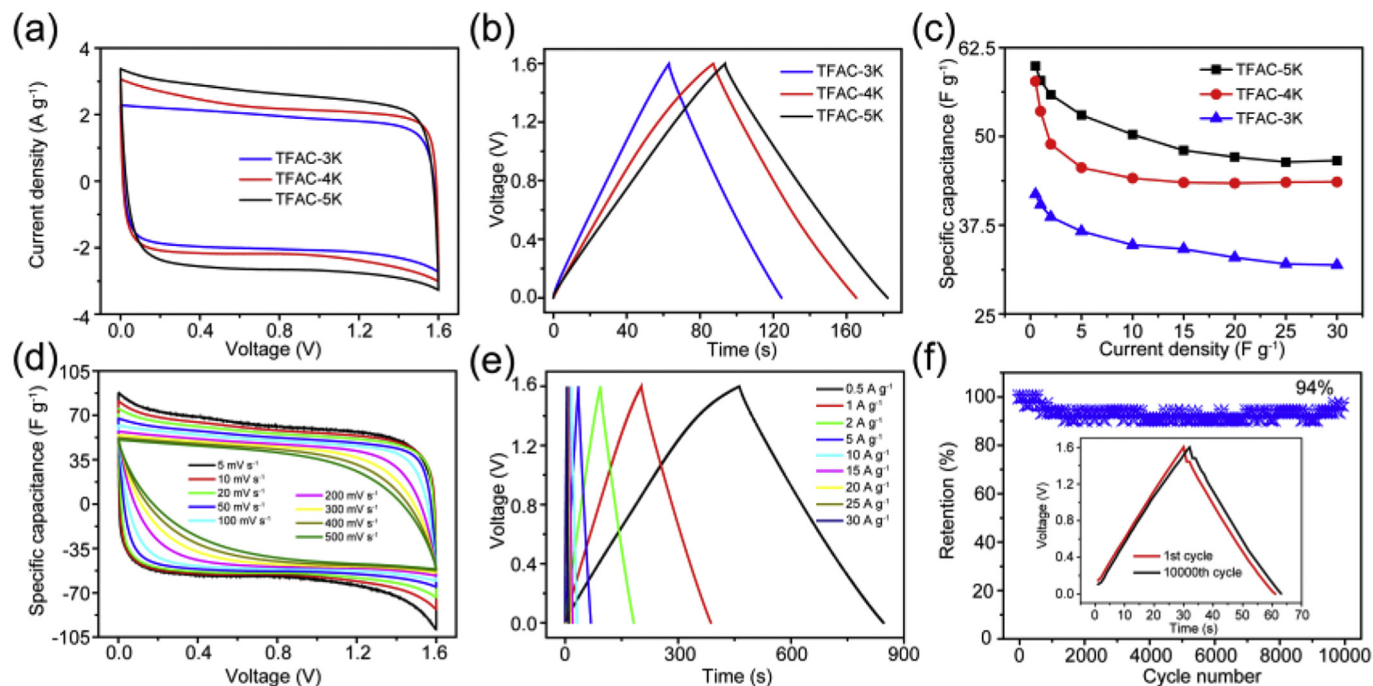


**Fig. 4.** (a) CV curves at  $50 \text{ mV s}^{-1}$ ; (b) GCD curves at  $2 \text{ A g}^{-1}$ ; (c) GCD rate performance of TFAC-3K, TFAC-4K and TFAC-5K in a symmetric two-electrode supercapacitor in  $1 \text{ M Na}_2\text{SO}_4$  aqueous solution; (d) CV curves at different sweep rates; (e) GCD curves at different current densities; (f) cyclic durability at  $5 \text{ A g}^{-1}$  for 10,000 cycles of TFAC-5K (inset: GCD curves of the 1st and 10 000th cycles).

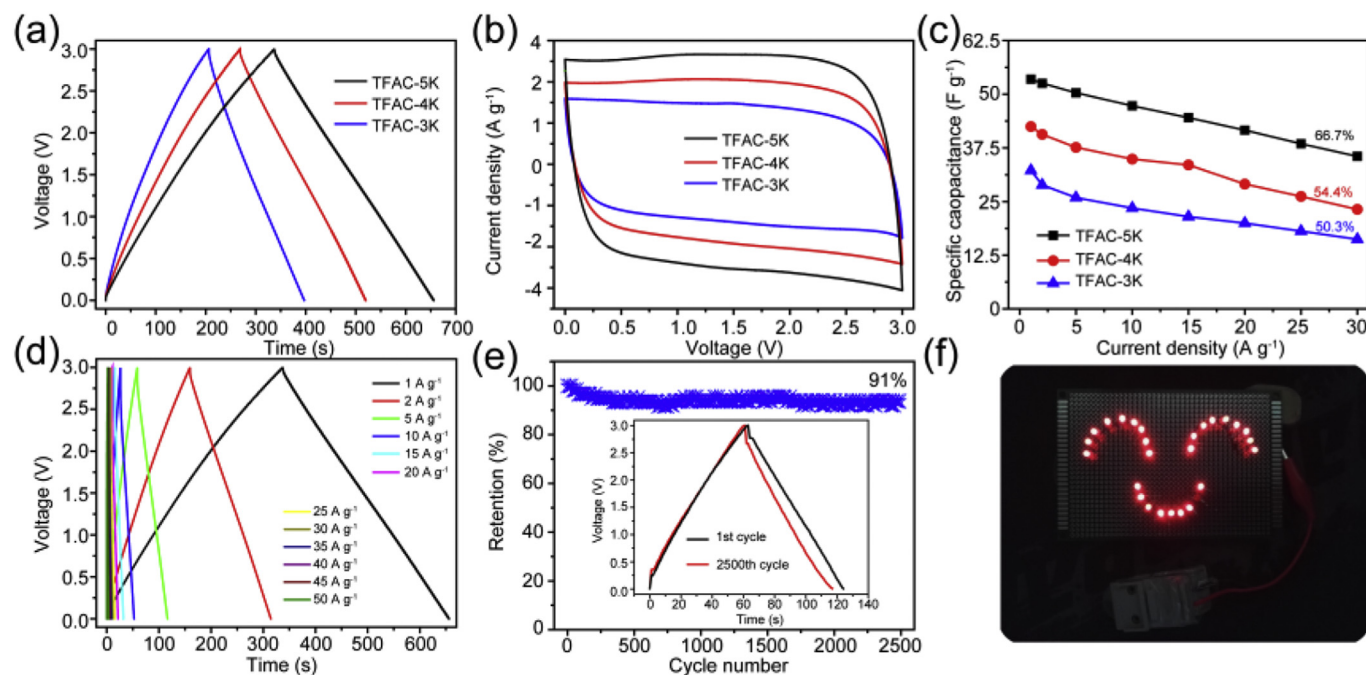


**Fig. 5.** (a) GCD curves at  $1 \text{ A g}^{-1}$ ; (b) CV curves at  $50 \text{ mV s}^{-1}$ ; (c) GCD rate performance of TFAC-3K, TFAC-4K and TFAC-5K in symmetric two-electrode supercapacitor in neat EMIM  $\text{BF}_4$ ; (d) GCD curves at various current densities; (e) cyclic stability at  $5 \text{ A g}^{-1}$  for 5000 cycles of TFAC-5K; (f) digital photograph of LEDs powered by the symmetric two-electrode capacitor of TFAC-5K.

accumulation [57]; (2) abundant mesopore can allow plentiful electrolyte ions to easily passing the pores and broader pore can effectively ease the ion “traffic jam” phenomenon in nanopores [58]. High SSA and abundant mesopore volume synergistically endow superior electrochemical performance of TFAC-5K based symmetrical SCs in EMIM  $\text{BF}_4$ .

EIS was measured to understand the ion diffusion process of TFAC-5K based SCs in different electrolytes. The Nyquist plots and the magnification in the high frequency in ionic liquid and aqueous systems are shown in Fig. 6a. At low frequency, the lines almost vertical to the real axis clearly suggest fast ion transport to the inner pores and perfect double layer capacitive property [56]. The first

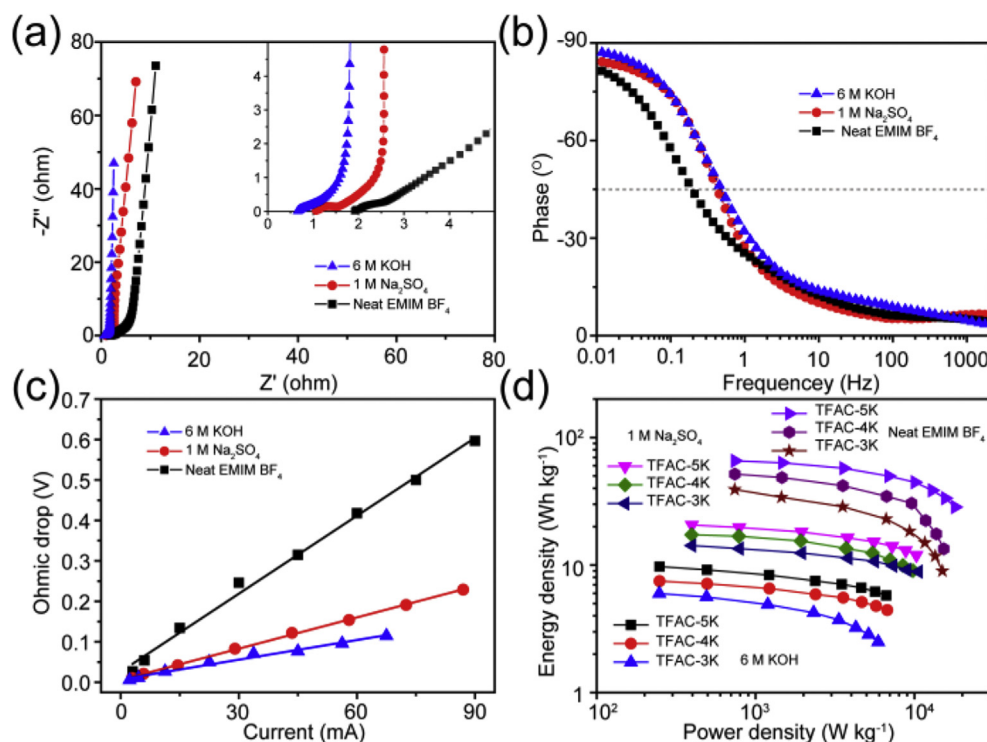


**Fig. 6.** (a) Nyquist plots (inset: magnification of the Nyquist plot); (b) the frequency response; (c) Ohmic drop associated with the equivalent internal resistance at various current densities for the TFAC-5K based supercapacitors in 6 M KOH, 1 M Na<sub>2</sub>SO<sub>4</sub> and EMIM BF<sub>4</sub>; (d) Ragone plots for the TFAC based supercapacitors in different electrolytes.

intercept value of real axis is the ohmic resistance which contains the resistance of the coin cell, current collector, active materials, contact resistance of active materials and current collector, separator and electrolytes [58]. The TFAC-5K based SCs show very low ohmic resistances of 1.9, 1.06 and 0.67  $\Omega$  for the neat EMIM BF<sub>4</sub>, 1 M Na<sub>2</sub>SO<sub>4</sub> and 6 M KOH, respectively (inset Fig. 6a). The small semi-circle at high frequency corresponds to low charge transfer resistances. The short 45° line at intermediate frequency indicates the low ion diffusion resistance due to the high mesopore ratio ensuring efficient ion transfer process [59]. Bode plots are presented in Fig. 6b. The frequencies ( $f_0$ , for a phase angle of  $-45^\circ$ ) are 0.21, 0.45, and 0.55 Hz for the neat EMIM BF<sub>4</sub>, 1 M Na<sub>2</sub>SO<sub>4</sub> and 6 M KOH system, respectively. The minimum time ( $\tau_0 = 1/f_0$ ), the energy be discharged with an efficiency >50% are 4.76 s (neat EMIM BF<sub>4</sub>), 2.22 s (1 M Na<sub>2</sub>SO<sub>4</sub>) and 1.81 (6 M KOH) which are much lower than commercial AC based supercapacitors (8–100 s) [59,60].

Energy density, is approximately proportional to  $V^2$  ( $V = V_{\max} - V_{\text{drop}}$ ) according to the equation  $E = CV^2/2$ , which means that the max operating voltage and ohmic drop ( $V_{\text{drop}}$ ) play very important role in energy delivery [3]. Fig. 6c shows the linear relationship between ohmic drop and current of TFAC-5K based SCs in different electrolytes. The slope of those lines represents equivalent resistances of the SCs [61]. The symmetric SC in 6 M KOH exhibits the smallest equivalent series resistance (1.62  $\Omega$ ), which is lower than that in 1 M Na<sub>2</sub>SO<sub>4</sub> (2.57  $\Omega$ ) and neat EMIM BF<sub>4</sub> (6.42  $\Omega$ ) due to the KOH possessing smallest hydrated ion size and highest ionic conductivity [1]. Fig. 6d shows the Ragone plots based on gravimetric basis in different electrolytes for the TFAC. The SCs in neat EMIM BF<sub>4</sub> show the higher energy density in spite of the lower capacitance than that in 6 M KOH and 1 M Na<sub>2</sub>SO<sub>4</sub>, which is attributed to the extended operating voltage (3 V). The maximum energy density of the TFAC-5K based SC in EMIM BF<sub>4</sub> is 65.6 W h kg<sup>-1</sup> at a power density of 743 W kg<sup>-1</sup>, which is much higher than that in 1 M Na<sub>2</sub>SO<sub>4</sub> (21.2 W h kg<sup>-1</sup> at 200 W kg<sup>-1</sup>), 6 M KOH (9.6 W h kg<sup>-1</sup> at

124 W kg<sup>-1</sup>), TFAC-4K, TFAC-3K and the state of art AC materials in ionic liquid and organic electrolytes (Table S3). Moreover, the energy density of 28 W h kg<sup>-1</sup> also maintain at 19,700 W kg<sup>-1</sup>. These results indicate that the TFAC-5K based symmetric EDLCs can simultaneously deliver ultrahigh power and energy density.

#### 4. Conclusion

In summary, hierarchical ACs with ultrahigh specific surface area were prepared through carbonization and subsequent KOH activation of tremella. Due to its ultrahigh surface area, large mesopore ratio and high surface oxygen content, the obtained supercapacitor shows high specific capacitances of 71 F g<sup>-1</sup> at 1 A g<sup>-1</sup> in 6 M KOH and 60 F g<sup>-1</sup> at 0.5 A g<sup>-1</sup> in 1 M Na<sub>2</sub>SO<sub>4</sub>, respectively, and excellent cycling durability of 99% and 94% capacitance retention at 5 A g<sup>-1</sup> after 10,000 cycles. More importantly, the as-assembled symmetric SC also delivers a superb energy density of 65.6 W h kg<sup>-1</sup> and 28 W h kg<sup>-1</sup> is still maintained even at ultrahigh power density 19,700 W kg<sup>-1</sup>. Therefore, employing sustainable biomaterials to prepare advanced activated carbon materials for high property SCs is a promising strategy.

#### Acknowledgment

The authors greatly acknowledge the financial support from the National Natural Science Foundation of China (51432003 and 51372012).

#### Appendix A. Supplementary data

Supplementary data related to this article can be found at <http://dx.doi.org/10.1016/j.matchemphys.2017.08.054>.



## References

- [1] J. Wang, P. Nie, B. Ding, S. Dong, X. Hao, H. Dou, X. Zhang, Biomass derived carbon for energy storage devices, *J. Mater. Chem. A* 5 (2017) 2411–2428.
- [2] J. Deng, M. Li, Y. Wang, Biomass-derived carbon: synthesis and applications in energy storage and conversion, *Green Chem.* 18 (2016) 4824–4854.
- [3] C. Zhong, Y. Deng, W. Hu, J. Qiao, L. Zhang, J. Zhang, A review of electrolyte materials and compositions for electrochemical supercapacitors, *Chem. Soc. Rev.* 44 (2015) 7484–7539.
- [4] A. Diviyashree, S.A.B.A. Shoriya, S. Yallappa, K. Chaitra, N. Kathyayini, G. Hedge, Low cost, high performance supercapacitor electrode using coconut wastes: eco-friendly approach, *J. Energy Chem.* 25 (2016) 880–887.
- [5] F. Bella, S. Galliano, M. Falco, G. Viscardi, C. Barolo, M. Grätzel, C. Gerbaldi, Approaching truly sustainable solar cells by the use of water and cellulose derivatives, *Green Chem.* 19 (2017) 1043–1051.
- [6] F. Bella, D. Pugliese, L. Zolin, C. Gerbaldi, Paper-based quasi-solid dye-sensitized solar cells, *Electrochim. Acta* 237 (2017) 87–93.
- [7] L. Zolin, J.R. Nair, D. Beneventi, F. Bella, M. Destro, P. Jagdale, I. Cannavaro, A. Tagliaferro, D. Chaussy, F. Geobaldo, C. Gerbaldi, A simple route toward next-gen green energy storage concept by nanofibres-based self-supporting electrodes and a solid polymeric design, *Carbon* 107 (2016) 811–822.
- [8] L.L. Zhang, X.S. Zhao, Carbon-based materials as supercapacitor electrodes, *Chem. Soc. Rev.* 38 (2009) 2520–2531.
- [9] Q. Wang, J. Yan, Z. Fan, Carbon materials for high volumetric performance supercapacitors: design, progress, challenges and opportunities, *Energy Environ. Sci.* 9 (2016) 729–762.
- [10] Y. Wang, Y. Song, Y. Xia, Electrochemical capacitors: mechanism, materials, systems, characterization and applications, *Chem. Soc. Rev.* 45 (2016) 5925–5950.
- [11] G.A. Ali, M.M. Yusoff, E.R. Shaaban, K.F. Chong, High performance MnO<sub>2</sub> nanoflower supercapacitor electrode by electrochemical recycling of spent batteries, *Ceram. Int.* 43 (2017) 8440–8448.
- [12] G.A. Ali, Fouad, S.A. Makhlof, M.M. Yusoff, K.F. Chong, Co<sub>3</sub>O<sub>4</sub>/SiO<sub>2</sub> nano-composites for supercapacitor application, *J. Solid State Electrochem* 18 (2014) 2505–2512.
- [13] E. Frackowiak, Carbon materials for supercapacitor application, *Phys. Chem. Chem. Phys.* 9 (2007) 1774–1785.
- [14] M. Shi, S. Kou, X. Yan, Engineering the electrochemical capacitive properties of graphene sheets in ionic-liquid electrolytes by correct selection of anions, *Chem. Sus Chem.* 7 (2014) 3053–3062.
- [15] A. Brandt, S. Pohlmann, A. Varzi, A. Balducci, S. Passerini, Ionic liquids in supercapacitors, *MRS Bull.* 38 (2013) 554–559.
- [16] F.B. Sillars, S.I. Fletcher, M. Mirzaei, P.J. Hall, Variation of electrochemical capacitor performance with room temperature ionic liquid electrolyte viscosity and ion size, *Phys. Chem. Chem. Phys.* 14 (2012) 6094–6100.
- [17] M. Armand, F. Endres, D.R. MacFarlane, H. Ohno, B. Scrosati, Ionic-liquid materials for the electrochemical challenges of the future, *Nat. Mater* 8 (2009) 621–629.
- [18] W. Tian, Q. Gao, Y. Tan, K. Yang, L. Zhu, C. Yang, H. Zhang, Bio-inspired beehive-like hierarchical nanoporous carbon derived from bamboo-based industrial byproduct as a high performance supercapacitor electrode material, *J. Mater. Chem. A* 3 (2015) 5656–5664.
- [19] X. Wang, H. Zhou, E. Sheridan, J.C. Walmsley, D. Ren, D. Chen, Geometrically confined favourable ion packing for high gravimetric capacitance in carbon-ionic liquid supercapacitors, *Energy Environ. Sci.* 9 (2016) 232–239.
- [20] L. Jiang, L. Sheng, X. Chen, T. Wei, Z. Fan, Construction of nitrogen-doped porous carbon buildings using interconnected ultra-small carbon nanosheets for ultra-high rate supercapacitors, *J. Mater. Chem. A* 4 (2016) 11388–11396.
- [21] D. He, J. Niu, M. Dou, J. Ji, Y. Huang, F. Wang, Nitrogen and oxygen co-doped carbon networks with a mesopore-dominant hierarchical porosity for high energy and power density supercapacitors, *Electrochim. Acta* 238 (2017) 310–318.
- [22] C. Long, X. Chen, L. Jiang, L. Zhi, Z. Fan, Porous layer-stacking carbon derived from in-built template in biomass for high volumetric performance supercapacitors, *Nano Energy* 12 (2015) 141–151.
- [23] J. Deng, T. Xiong, F. Xu, M. Li, C. Han, Y. Gong, H. Wang, Y. Wang, Inspired by bread leavening: one-pot synthesis of hierarchically porous carbon for supercapacitors, *Green Chem.* 17 (2015) 4053–4060.
- [24] Y. Rangom, X. Tang, L.F. Nazar, Carbon nanotube-based supercapacitors with excellent ac line filtering and rate capability via improved interfacial impedance, *ACS Nano* 9 (2015) 7248–7255.
- [25] G.A. Ali, E.Y.L. Teo, E.A.A. Aboelazm, H. Sadegh, A.O.H. Memar, R. Shahryari-Ghosheh, K.F. Chong, Capacitive performance of cysteamine functionalized carbon Nanotubes, *Mater. Chem. Phys.* 197 (2017) 100–104.
- [26] A.B. Furtess, G. Lota, T.A. Centeno, E. Frackowiak, Templated mesoporous carbons for supercapacitor application, *Electrochim. Acta* 14 (2005) 2799–2805.
- [27] Y. Kado, K. Imoto, Y. Soneda, N. Yoshizawa, Correlation between the pore structure and electrode density of MgO-templated carbons for electric double layer capacitor applications, *J. Power Sources* 305 (2016) 128–133.
- [28] M. Oschatz, S. Boukhalfa, W. Nickel, J.P. Hofmann, C. Fischer, G. Yushin, S. Kaskel, Carbide-derived carbon aerogels with tunable pore structure as versatile electrode material in high power supercapacitors, *Carbon* 113 (2017) 283–291.
- [29] X.X. Lin, B. Tan, L. Peng, Ionothermal synthesis of microporous and mesoporous carbon aerogels from fructose as electrode materials for supercapacitors, *J. Mater. Chem. A* 4 (2016) 4497–4505.
- [30] C. Liu, Z. Yu, D. Neff, A. Zhamu, B.Z. Jang, Graphene-based supercapacitor with an ultrahigh energy density, *Nano Lett.* 10 (2010) 4863–4868.
- [31] P.E. Marina, G.A.M. Ali, L.M. See, E.Y.L. Teo, E.P. Ng, K.F. Chong, In situ growth of redox-active iron-centered nanoparticles on graphene sheets for specific capacitance enhancement, *Arab. J. Chem.* (2016), <http://dx.doi.org/10.1016/j.arabj.2016.02.006>.
- [32] G.A. Ali, S.A. Makhlof, M.M. Yusoff, K.F. Chong, Structural and electrochemical characteristics of graphene nanosheets as supercapacitor electrodes, *Rev. Adv. Mater. Sci.* 41 (2015) 35–43.
- [33] Z. Li, Z. Xu, X. Tan, H. Wang, C.M.B. Holt, T. Stephenson, B.C. Olsen, Mesoporous nitrogen-rich carbons derived from protein for ultra-high capacity battery anodes and supercapacitors, *Energy Environ. Sci.* 6 (2013) 871–878.
- [34] M.H. Sun, S.Z. Huang, L.H. Chen, Y. Li, X.Y. Yang, Z.Y. Yuan, B.L. Su, Applications of hierarchically structured porous materials from energy storage and conversion, catalysis, photocatalysis, adsorption, separation, and sensing to biomedicine, *Chem. Soc. Rev.* 45 (2016) 3479–3563.
- [35] H. Feng, H. Hu, H. Dong, Y. Xiao, Y. Cai, B. Lei, Y. Liu, M. Zheng, Hierarchical structured carbon derived from bagasse wastes: a simple and efficient synthesis route and its improved electrochemical properties for high-performance supercapacitors, *J. Power Sources* 302 (2016) 164–173.
- [36] X. Wen, D. Zhang, T. Yan, J. Zhang, L. Shi, Three dimensional graphene-based hierarchically porous carbon composites prepared by a dual-template strategy for capacitive deionization, *J. Mater. Chem. A* 1 (2013) 12334–12344.
- [37] P. Avetta, F. Bella, A. Bianco Prevot, E. Laurenti, E. Montoneri, A. Arques, L. Carlos, Waste cleaning waste: photodegradation of monochlorophenols in the presence of waste-derived photosensitizer, *ACS Sustain. Chem. Eng.* 1 (2013) 1545–1550.
- [38] N. Guo, M. Li, Y. Wang, X. Sun, F. Wang, R. Yang, Soybean root-derived hierarchical porous carbon as electrode material for high-performance supercapacitors in ionic liquids, *ACS Appl. Mater. Interfaces* 8 (2016) 33626–33634.
- [39] C. Chen, Y. Zhang, Y. Li, J. Dai, J. Song, Y. Yao, Y. Gong, I. Kierzewski, J. Xie, L. Hu, All-wood, low tortuosity, aqueous, biodegradable supercapacitors with ultra-high capacitance, *Energy Environ. Sci.* 10 (2017) 538–545.
- [40] H. Tan, X. Wang, D. Jia, P. Hao, Y. Sang, H. Liu, Structure-dependent electrode properties of hollow carbon micro-fibers derived from platanus fruit and willow catkins for high-performance supercapacitors, *J. Mater. Chem. A* 5 (2017) 2580–2591.
- [41] Y.Q. Zhao, M. Lu, P.Y. Tao, Y.J. Zhang, X.T. Gong, Z. Yang, G.Q. Zhang, H.L. Li, Hierarchically porous and heteroatom doped carbon derived from tobacco rods for supercapacitors, *J. Power Sources* 307 (2016) 391–400.
- [42] W. Yu, H. Wang, S. Liu, N. Mao, X. Liu, J. Shi, W. Liu, S. Chen, X. Wang, N. O-codoped hierarchical porous carbons derived from algae for high-capacity supercapacitors and battery anodes, *J. Mater. Chem. A* 4 (2016) 5973–5983.
- [43] B. Hu, K. Wang, L. Wu, S.H. Yu, M. Antonietti, M.M. Titirici, Engineering carbon materials from the hydrothermal carbonization process of biomass, *Adv. Mater* 22 (2010) 813–828.
- [44] H. Zhu, X. Wang, F. Yang, X. Yang, Promising carbons for supercapacitors derived from fungi, *Adv. Mater* 23 (2011) 2745–2748.
- [45] J. Li, K. Liu, X. Gao, B. Yao, K. Huo, Y. Cheng, X. Cheng, D. Chen, B. Wang, W. Sun, D. Ding, M. Liu, L. Huang, Oxygen-and nitrogen-enriched 3D porous carbon for supercapacitors of high volumetric capacity, *ACS Appl. Mater. Interfaces* 7 (2015) 24622–24628.
- [46] P. Khondkar, K.E. Aidoo, R.F. Tester, Sugar profile of extracellular polysaccharides from different tremella species, *Int. J. Food Microbiol.* 79 (2002) 121–129.
- [47] J. Liu, C.G. Meng, Y.H. Yan, Y.N. Shan, J. Kan, C.H. Jin, Structure, physical property and antioxidant activity of catechin grafted tremella fuciformis polysaccharide, *Int. J. Biol. Macromol.* 82 (2016) 719–724.
- [48] M.M. Titirici, M. Antonietti, Chemistry and materials options of sustainable carbon materials made by hydrothermal carbonization, *Chem. Soc. Rev.* 39 (2010) 103–116.
- [49] R. Mysyk, Q. Gao, E. Raymundo-Pinero, F. Béguin, Microporous carbons finely-tuned by cyclic high-pressure low-temperature oxidation and their use in electrochemical capacitors, *Carbon* 50 (2012) 3367–3374.
- [50] L. Zhang, F. Zhang, X. Yang, K. Leng, Y. Huang, Y. Chen, High-performance supercapacitor electrode materials prepared from various pollens, *Small* 9 (2013) 1342–1347.
- [51] Y.S. Yun, G. Yoon, K. Kang, H.J. Jin, High-performance supercapacitors based on defect-engineered carbon nanotubes, *Carbon* 80 (2014) 246–254.
- [52] Y.S. Yun, V.D. Le, H. Kim, S.J. Chang, S.J. Baek, S. Park, B.H. Kim, Y.H. Kim, K. Kang, H.J. Jin, Effects of sulfur doping on graphene-based nanosheets for use as anode materials in lithium-ion batteries, *J. Power Sources* 262 (2014) 79–85.
- [53] Y. Wang, R. Yang, M. Li, Z. Zhao, Hydrothermal preparation of highly porous carbon spheres from hemp (*Cannabis sativa* L.) stem hemicellulose for use in energy-related applications, *Ind. Crop. Prod.* 65 (2015) 216–226.
- [54] L. Qie, W. Chen, H. Xu, X. Xiong, Y. Jiang, F. Zou, X. Hu, Y. Xin, Z. Zhang, Y. Huang, Synthesis of functionalized 3D hierarchical porous carbon for high-performance supercapacitors, *Energy Environ. Sci.* 6 (2013) 2497–2504.
- [55] H. Liu, H. Song, X. Chen, S. Zhang, J. Zhou, Z. Ma, Effects of nitrogen- and oxygen-containing functional groups of activated carbon nanotubes on the



- electrochemical performance in supercapacitors, *J. Power Sources* 285 (2015) 303–309.
- [56] H. Wang, Z. Xu, A. Kohandehghan, Z. Li, K. Cui, X. Tan, T.J. Stephenson, C.K. King'ondo, C.M.B. Holt, B.C. Olsen, J.K. Tak, D. Harfield, A.O. Anyia, D. Mitlin, Interconnected carbon nanosheets derived from hemp for ultrafast supercapacitors with high energy, *ACS Nano* 7 (2013) 5131–5141.
- [57] W. Li, J. Liu, D. Zhao, Mesoporous materials for energy conversion and storage devices, *Nat. Rev. Mater* 1 (2016) 16023–16040.
- [58] W. Tian, Q. Gao, Y. Tan, K. Yang, L. Zhu, C. Yang, H. Zhang, Bio-inspired beehive-like hierarchical nanoporous carbon derived from bamboo-based industrial byproduct as a high performance supercapacitor electrode material, *J. Mater. Chem. A* 3 (2015) 5656–5664.
- [59] M. Sevilla, A.B. Fuertes, Direct synthesis of highly porous interconnected carbon nanosheets and their application as high-performance supercapacitors, *ACS Nano* 8 (2014) 5069–5078.
- [60] L. Wei, M. Sevilla, A.B. Fuertes, R. Mokaya, G. Yushin, Hydrothermal carbonization of abundant renewable natural organic chemicals for high-performance supercapacitor electrodes, *Adv. Energy Mater* 1 (2011) 356–361.
- [61] X. Wei, S. Wan, X. Jiang, Z. Wang, S. Gao, Peanut-shell-like porous carbon from nitrogen-containing poly-n-phenylethanolamine for high-performance supercapacitor, *ACS Appl. Mater. Interfaces* 7 (2015) 22238–22245.